

Supplementary Information

Nuclear quantum effects in two-hydrogen intermediates on graphene-embedded transition metal atoms

Erxun Han,^{1,2} Wei Fang,^{3,*} and Ji Chen^{1,2,4,†}

¹*School of Physics, Peking University, Beijing 100871, China*

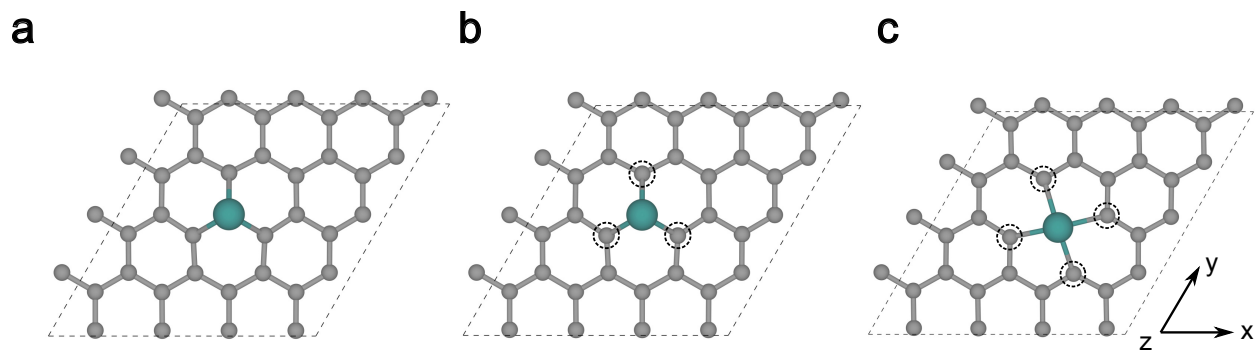
²*Interdisciplinary Institute of Light-Element Quantum Materials
and Research Center for Light-Element Advanced Materials,
Peking University, Beijing 100871, People's Republic of China*

³*Department of Chemistry, Shanghai Key Laboratory
of Molecular Catalysis and Innovative Materials,
Fudan University, Shanghai 200438, P. R. China*

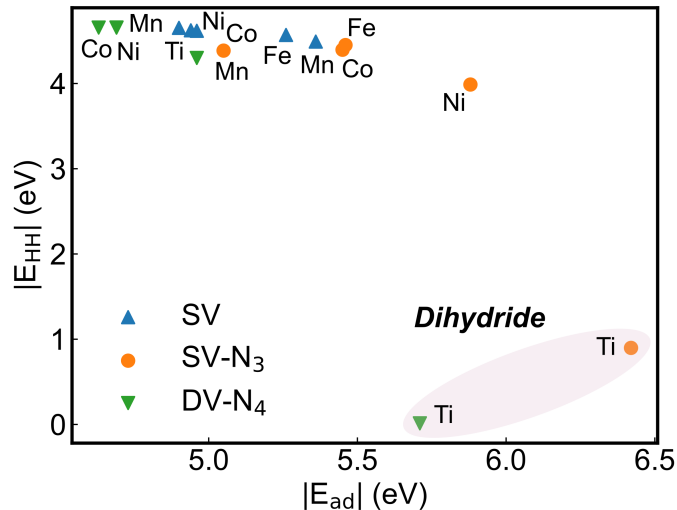
⁴*Frontiers Science Center for Nano-Optoelectronics,
Peking University, Beijing 100871, People's Republic of China*

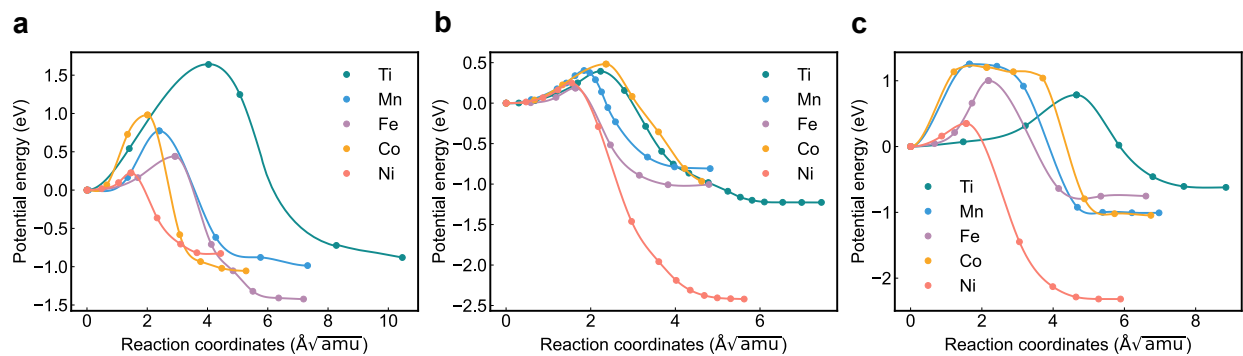
* wei.fang@fudan.edu.cn

† ji.chen@pku.edu.cn

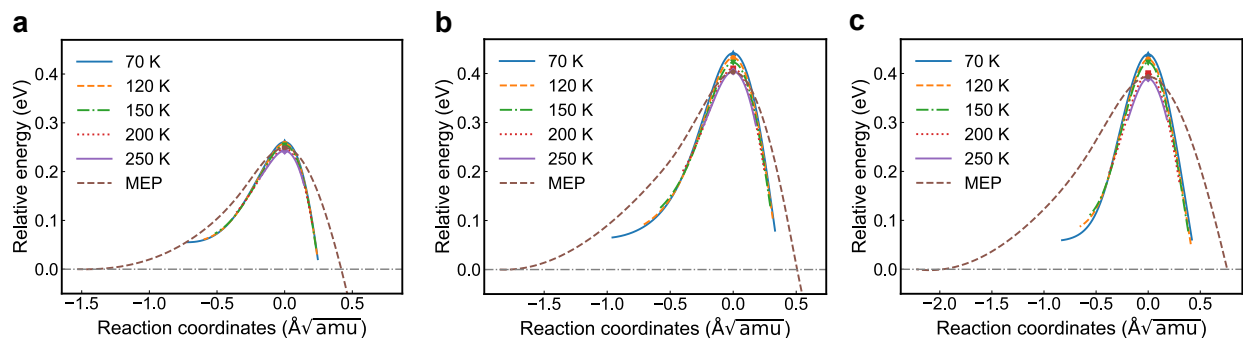


Supplementary Figure 1. The graphene-embedded metal atoms investigated in this work include the following three defective graphene supports: (a) single vacancy (SV), (b) nitrogen-substituted single vacancy (SV-N₃), and (c) nitrogen-substituted double vacancy (DV-N₄). The metal atom candidates are Ti, Mn, Fe, Co, and Ni. In the models, carbon atoms are colored gray, and metal atoms are colored green. The carbon atoms, highlighted with black dashed circles, are replaced by nitrogen atoms.





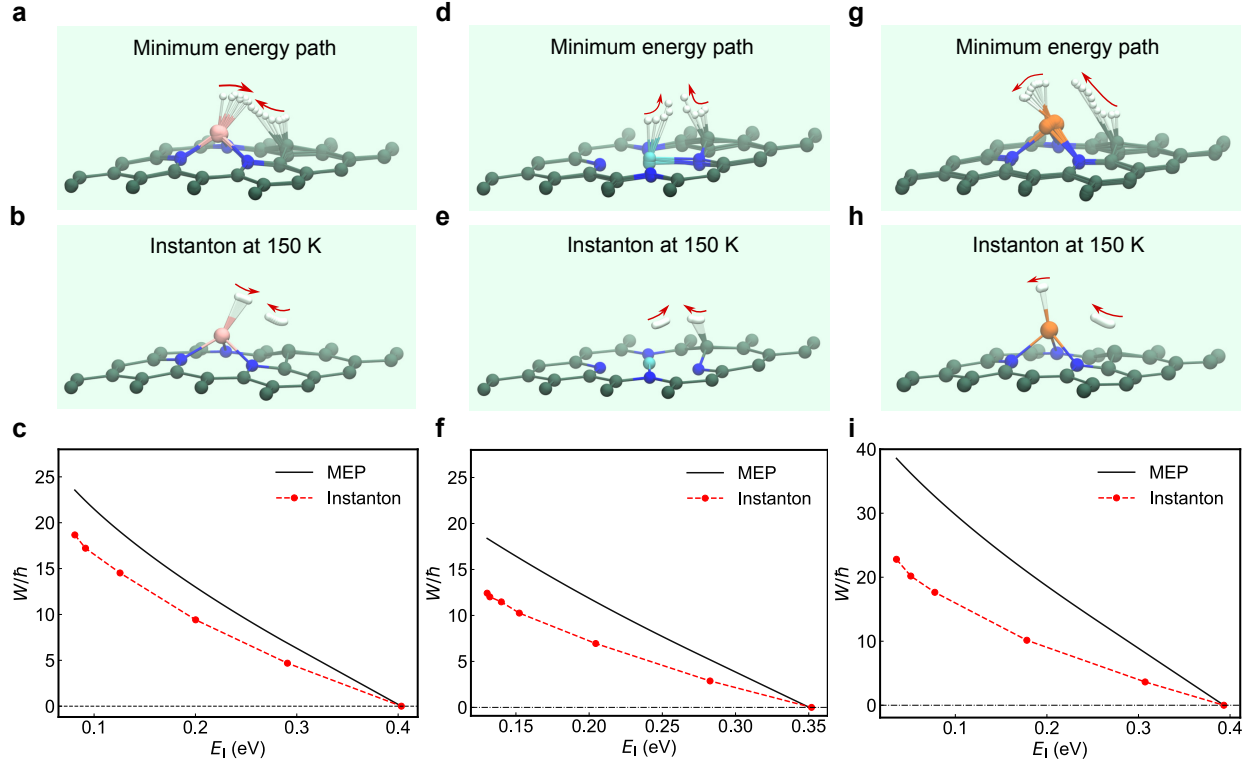
Supplementary Figure 3. Potential energy profiles in mass-weighted coordinates for the formation of two-hydrogen intermediates on various graphene-embedded metal atoms, calculated using the CI-NEB method: (a) on SV, (b) on SV- N_3 , and (c) on DV- N_4 . Most processes exhibit small energy barriers below 1.0 eV. Due to their exothermic nature, the formation of two-hydrogen intermediates is predicted to occur rapidly.



Supplementary Figure 4. Instanton trajectories in mass-weighted coordinates of two-hydrogen intermediate formation processes on (a) Ni@DV-N₄, (b) Mn@SV-N₃ and (c) Ti@SV-N₃. MEPs are also provided for direct comparison.

Supplementary note in Supplementary Figure 4

The multidimensional tunneling also affects the quantum rate constant enhancement, namely, the “corner-cutting effect” where the quantum tunneling pathway deviates from the classical MEP. In earlier studies, the corner-cutting effects in one-dimensional tunneling computations were undetectable until the instanton method was extended to multidimensional space. The calculated instantons for selected intermediates are illustrated in Supplementary Fig. 4. As the temperature decreases, the instanton extends from the transition state to the low energy region. Meanwhile, their peak regions climb higher and gradually deviate from MEP. At 70 K, the instanton is fully stretched, reaching the deep tunneling region.



Supplementary Figure 5. MEPs, instanton trajectories (150 K), and the abbreviated action W computed for (a–c) binding dihydrogen (BDH) formation on Mn@SV-N₃, (d–f) physisorbed dihydrogen (PDH) formation on Ni@DV-N₄, and (g–i) dihydride formation on Ti@SV-N₃.

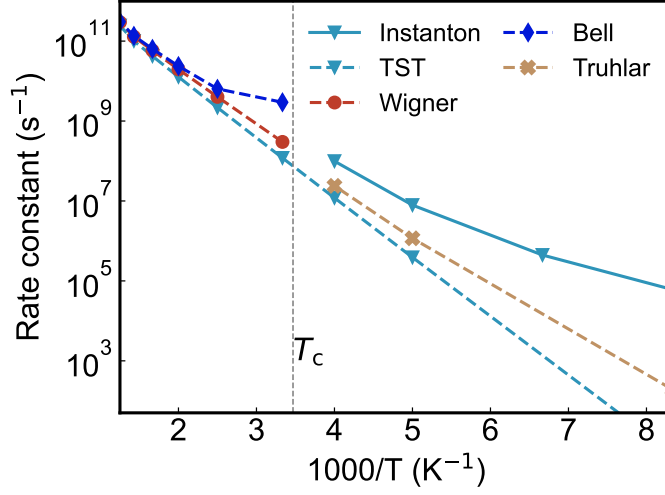
Supplementary note in Supplementary Figure 5

The deviation of instanton trajectories from MEPs can be quantified by the abbreviated action W , defined as:

$$W = 2 \int_{\mathbf{x}} \sqrt{2(V(q) - E)} \, dq \quad (1)$$

where \mathbf{x} is a given reaction path, $V(q)$ is the potential energy along the path and q is the mass-weighted coordinate. The calculated results of W are provided in Supplementary Fig. 5 c,f,i.

Generally, the abbreviated action W computed along instanton is below that along MEPs, showing more quantum corner-cutting effects at low temperatures. For dihydrogen and BDH formation processes, they have similar W differences because of their parallel H recombination behaviors around the transition state, where two H atoms desorb concertedly. However, in dihydride formation, the metal atom contributes less to the quantum tunneling pathways, while in MEPs it migrates some distance.



Supplementary Figure 6. Rate constants of BDH (Mn@SV-N₃) formation process with various tunneling corrections (Wigner, Bell, and Truhlar).

Supplementary note in Supplementary Figure 6

Wigner's correction is a simple first-order correction. A correction factor is applied to results from classical transition state theory:

$$\kappa = 1 + \frac{1}{24} \left(\frac{\hbar|\omega^\ddagger|}{k_B T} \right)^2, \quad (2)$$

where ω^\ddagger is the imaginary frequency of the transition state.

Bell's correction accounts for tunneling over a range of energies below the barrier top, with a correction factor:

$$\kappa = \frac{\hbar\omega^\ddagger/2k_B T}{\sin(\hbar\omega^\ddagger/2k_B T)}. \quad (3)$$

Truhlar's correction refines tunneling by considering the multidimensional nature of the PES. Its zero-curvature tunneling correction factor used in this work is:

$$\kappa = \frac{\int_0^\infty P(E) e^{-E/k_B T} dE}{\int_{V^\ddagger}^\infty e^{-E/k_B T} dE} \quad (4)$$

$$P(E) = \exp \left(-\frac{2}{\hbar} \int_a^b \sqrt{2\mu(V(x) - E)} dx \right) \quad (5)$$

where V^\ddagger is the energy barrier of a given reaction and $V(x)$ is the minimum energy pathway.

As a brief illustration, we compare several rate constants of BDH (Mn@DV-N₃) formation process with quantum tunneling corrections based on the parabolic barrier. Among these results, Wigner's and Bell's corrections only apply for shallow tunneling regimes, making

them applicable at temperatures above T_c . Bell's correction diverges at T_c , while Wigner's correction will seriously underestimate the tunneling at temperatures below T_c . Overall, both of them show minimal improvement over TST predictions. Additionally, Truhlar's zero-curvature tunneling correction consistently underestimates tunneling effects compared with *ab initio* instanton results, because it fails to account for the corner-cutting effect. In contrast, *ab initio* instanton theory explicitly accounts for this effect, thereby predicting tunneling more accurately. These comparisons further highlight the complex nature of tunneling and the different roles of each correction.

Supplementary Table I. Bader charge (in e) for adsorbed H atoms and metal atom. Charge transfer values with respect to the free atoms are provided in brackets, where a positive value means electron gain.

	H	H	Metal atom
Mn@SV-N ₃	1.07 (+0.07)	1.09 (+0.09)	6.12 (−0.88)
Ti@SV-N ₃	1.43 (+0.43)	1.50 (+0.50)	2.32 (−1.68)
Ni@DV-N ₄	1.00 (0)	1.00 (0)	9.12 (−0.88)

Supplementary Table II. Potential energy barriers (ΔE s, identical to Supplementary Figure 3), and crossover temperatures (T_c s) for the formation processes of two-hydrogen intermediates.

	ΔE s (eV)/ T_c s (K)		
	SV	SV-N ₃	DV-N ₄
Ti	1.63/220.5	0.39/299.3	0.79/255.1
Mn	0.77/318.0	0.41/288.3	1.25/76.7
Fe	0.44/352.1	0.19/283.2	1.00/397.9
Co	0.98/294.2	0.48/200.0	1.20/59.4
Ni	0.22/278.9	0.44/363.9	0.25/285.8

Supplementary Table III. Details of *ab initio* instanton calculations.

Catalysts	Temperature (K)	N bead instanton rate constant (s^{-1})	Beads	W/\hbar	E_{I} (eV)
Mn@SV-N ₃	70	2.09×10^2	128	30.48	0.07
	100	9.75×10^3	128	28.41	0.09
	120	6.07×10^4	64	26.21	0.10
	150	4.44×10^5	64	22.16	0.14
	200	7.88×10^6	32	14.45	0.21
	250	9.90×10^7	20	7.27	0.30
Ti@SV-N ₃	70	2.67×10^4	128	22.8	0.04
	100	7.92×10^5	128	21.53	0.041
	120	2.70×10^6	64	20.19	0.05
	150	1.72×10^7	64	17.64	0.08
	200	1.65×10^8	32	10.60	0.18
	250	8.43×10^8	20	3.64	0.31
Ni@DV-N ₄	70	1.71×10^7	128	14.20	0.12
	100	2.55×10^8	128	13.50	0.13
	120	7.96×10^8	64	12.54	0.14
	150	4.06×10^9	64	11.14	0.15
	200	3.81×10^{10}	32	7.34	0.20
	250	2.16×10^{11}	20	3.04	0.28

Supplementary Table IV. *Ab initio* instanton rate constants for D₂ and HD formation reactions at 100 K.

Catalysts	<i>Ab initio</i> instanton rate constants (s ⁻¹)	
	HD	D ₂
Mn@SV-N ₃	6.81×10^{-1}	3.45×10^{-5}
Ti@SV-N ₃	6.53×10^2	2.11×10^{-1}
Ni@DV-N ₄	7.57×10^4	2.39×10^2